Radiation-Hydrodynamics, Spectral, and Atomic Physics Modeling of Laser-Produced Plasma EUV Lithography Light Sources

J. J. MacFarlane[1], C. L. Rettig[1], P. Wang[1], I. E. Golovkin[1], and P. R. Woodruff[1]

[1] Prism Computational Sciences, Inc., Madison, WI 53711, USA
[2] Cymer, Inc., San Diego, CA 92127

ABSTRACT

Tin, lithium, and xenon laser-produced plasmas are attractive candidates as light sources for extreme ultraviolet lithography (EUVL). Simulation of the dynamics and spectral properties of plasmas created in EUVL experiments plays a crucial role in analyzing and interpreting experimental measurements, and in optimizing the 13.5 nm radiation from the plasma source. Developing a good understanding of the physical processes in EUVL plasmas is challenging, as it requires accurate modeling for the atomic physics of complex atomic systems, frequency-dependent radiation transport, hydrodynamics, and the ability to simulate emergent spectra and images that can be directly compared with experimental measurements. We have developed a suite of plasma and atomic physics codes to simulate in detail the radiative properties of hot plasmas. HELIOS-CR is a 1-D radiation-magnetohydrodynamics code used to simulate the dynamic evolution of laser-produced and *z*-pinch plasmas. Multi-frequency radiation transport can be computed using either flux-limited diffusion or multi-angle models. HELIOS-CR also includes the capability to perform in-line non-LTE atomic kinetics calculations at each time step in the simulation. Energy source modeling includes laser energy deposition, radiation from external sources, and current discharges. The results of HELIOS-CR simulations can be post-processed using SPECT3D to generate images and spectra that include instrumental effects, and therefore can be directly compared with experimental measurements. Results from simulations of Sn laser-produced plasmas are presented, along with comparisons with experimental data. We discuss the sensitivity of the 13.5 nm conversion efficiency to laser intensity, wavelength, and pulse width, and show how the thickness of the Sn radiation layer affects the characteristics of the 13.5 nm emission.

Keywords: Atomic physics, radiation-hydrodynamics, EUV lithography, atomic spectroscopy, laser-produced plasmas, spectral analysis, radiation transport.

1. INTRODUCTION

Next-generation semiconductor chip manufacturing based on extreme ultraviolet lithography (EUVL) will require bright, efficient radiation sources at wavelengths near 13.5 nm.[1] Research on 13.5 nm EUV sources is actively being carried out by light source suppliers, research consortiums, and university research groups worldwide.[2-16] Development of high-power, highly efficient radiation sources is a critical issue that impacts both the technical and economic viability of EUVL systems. In addition, the type of source (composition, geometry, total mass ablated) can affect the overall lifetime and robustness of EUVL systems, as target debris can potentially damage components of the optics system.

EUVL requires radiation sources with strong emission in a narrow wavelength band ($\Delta\lambda / \lambda$ ~ 2%) near 13.5 nm. This requirement is driven by the use of Mo-Si multilayer mirrors in the collection optics of EUVL systems. EUVL sources must be efficient, debris-free, and capable of providing power levels of ~ 100 W in the 13.5 nm band. It is expected that laser-produced plasma (LPP) EUVL systems will operate at repetition rates of 5 - 10 kHz. To produce the needed power levels and to be economically viable, the 13.5 nm conversion efficiencies (*i.e.*, the ratio of the in-band 13.5 nm power to the incident laser power on target) of LPP EUVL sources must, at a minimum, achieve levels ~ several percent.

Achieving even higher conversion efficiencies reduces requirements for EUVL laser systems (shot repetition rate, total power usage), thereby reducing capital and maintenance costs associated with the system. In addition, more efficient sources, by reducing repetition rate requirements, reduce the total amount of target debris, and therefore lower the potential damage to the EUVL optics system. It is also advantageous to have more options for target material composition, as some materials are more likely to inflict damage to the wafer due to excessive amounts of out-of-band emission.

Several target materials are being studied as possible candidates for EUVL radiation sources, including xenon (Xe), tin (Sn), and lithium (Li). The motivation for using these materials is based on their atomic properties. Doubly-ionized lithium (Li^{2+}) exhibits strong Ly-α ($2p$-$1s$) emission at 13.5 nm. Xenon, at plasma temperatures and densities relevant to EUVL radiation sources, emits radiation near 13.5 nm primarily due to $5p$ - $4d$ transitions in ionization stages ranging from ~ Xe^{9+} to Xe^{11+}. Similarly, tin radiation near 13.5 nm arises from $4f$ - $4d$ and $4d$ - $4p$ transitions in ions from ~ Sn^{6+} to ~ Sn^{19+}. For Xe, the dominant radiation emission feature is near 10.5 nm, and the relatively small 13.5 nm feature has contributions from only a few ionization stages. For tin, the dominant emission feature is at 13.5 nm, and has contributions from a wider range of ionization stages. Materials with high atomic number ("high Z"), such as Sn and Xe, tend to emit radiation in unresolved transitions arrays (UTAs) due to the fact that they have many bound electrons and a large number of closely packed atomic energy levels. A single UTA typically emits light in a relatively broad wavelength band which includes a very large number of bound-bound transitions between two electronic configurations. High-Z materials also can efficiently convert laser energy into radiation, but much of that radiation is emitted outside of the 13.5 nm band useful for EUVL systems. This both reduces the 13.5 nm conversion efficiency and produces light at longer wavelengths that can have undesirable effects on the wafer. Lithium, because it has relatively few bound electrons, converts less of the laser energy into radiation, but of the radiation emitted, a significant fraction can be in the 13.5 nm band when the Li is highly ionized.

The radiative properties of plasmas created in LPP experiments depend both on the target properties and the laser beam properties. The plasma heating strongly depends on the laser intensity – not only its peak value, but also the time history of the intensity profile. The laser wavelength also affects the plasma heating, as shorter wavelength laser light tends to penetrate deeper into the plasma. The target composition, its geometry, and its initial state (*e.g.*, liquid droplets, planar foils, gas or liquid jets) also play a significant role in the evolution of plasma conditions and radiative output in EUVL LPP experiments.

Plasma simulation tools play a key role in developing a good understanding of the physical processes occurring in EUVL experiments. In evaluating the efficiency of 13.5 nm radiation in LPP and discharge-produced plasma (DPP) sources, it is critical to be able to accurately predict the frequency-dependent radiative emission from these sources. In addition, comparison with experimental data is a required step in assessing the accuracy of the modeling, and thereby assessing our level of understanding of the dominant physical processes occurring in these radiation sources.

Below, we describe computational tools designed to simulate in detail the atomic, radiative, and hydrodynamic properties of short-wavelength radiation sources. Results from Sn laser-produced plasma simulations are discussed, along with comparisons with experimental data. Measurement of Li conversion efficiencies and supporting modeling have been presented elsewhere.[3,6] We also present results showing the sensitivity of 13.5 nm conversion efficiency to laser wavelength, intensity, and pulse length.

2. RADIATION-HYDRODYNAMICS AND SPECTRAL MODELING

Below, we discuss results from calculations performed using a suite of plasma simulation tools.[17] These tools include: (1) a 1-D radiation-magnetohydrodynamics code; (2) a multi-dimensional imaging and spectral analysis code used to

post-process output from hydrodynamics simulations in order to make direct comparisons between simulations and experimental measurements; and (3) a spectral analysis code used to compute the radiative properties of finite-size single-cell plasmas of uniform temperature and density, and to determine representative temperatures and densities based on fits to experimental spectra. In this section, we briefly describe each of these simulation tools.

HELIOS is a 1-D Lagrangian radiation-magnetohydrodynamics code designed to simulate the evolution of a wide variety of high energy density plasmas.[18] HELIOS-CR is a version of HELIOS that includes the capability to perform inline non-LTE atomic kinetics (LTE* = local thermodynamic equilibrium) calculations at each time step in the hydrodynamics simulation. This inline collisional-radiative option has been used to study non-LTE effects in Li EUVL experiments.[13] HELIOS-CR solves the equation of motion for a single fluid. Electrons and ions are assumed to be co-moving. Pressure contributions to the equation of motion come from electrons, ions, radiation, and the magnetic field. Energy transport in the plasma can be treated using either a one-temperature ($T_e = T_i$) or two-temperature ($T_e \neq T_i$) model. Both the electrons and ions are assumed to have Maxwellian distributions defined by their respective temperatures, T_e and T_i. Options for thermal conduction models include: Spitzer conductivities, uniform (user-specified) material-dependent conductivities, and a hybrid Spitzer-uniform model.

Material equation of state (EOS) properties are based on either SESAME tables[19] or PROPACEOS tables.[18] Opacities are based either on tabulated multi-group (*i.e.,* frequency binned) PROPACEOS data, or, in the case when inline collisional-radiative modeling is used, frequency-dependent opacities based on non-LTE atomic level populations. In the latter case, an adaptive frequency mesh is used so that the structure near bound-bound transitions and bound-free edges is resolved. Radiation emission and absorption terms are coupled to the electron temperature equation. Multi-frequency radiation intensities are computed using either a flux-limited radiation diffusion model, or a multi-angle model based on the method of short characteristics.

Laser energy deposition is computed using an inverse Bremsstrahlung model, with the restriction that no energy in the beam passes beyond the critical surface. In planar geometry, laser light is transported along a single ray with incidence angle θ. In spherical geometry, a multi-ray, conical beam model is used. A magnetic diffusion model has recently been added to HELIOS-CR for calculations in cylindrical geometry. This provides the capability to simulate *z*-pinch plasmas created by current discharges.

The SPECT3D and PrismSPECT[22] codes utilize the same physics algorithms, but are used for different purposes. The SPECT3D package computes filtered and monochromatic images, and streaked, time-integrated, and time-gated spectra based on 1-D, 2-D, or 3-D radiation-hydrodynamics results. Simulated images and spectra can be computed with instrumental effects included (*e.g.*, spectrometer resolution, time gating, filtering) in order to facilitate comparisons with experimental data. SPECT3D is currently used to post-process output from HELIOS-CR and other radiation-hydrodynamics codes to analyze data obtained from a variety of laser-produced plasma and z-pinch plasma experiments being performed at the Univ. of Rochester OMEGA laser facility and the Sandia Z pulsed-power facility.

PrismSPECT computes the ionization dynamics and spectral properties of single-cell plasmas (*i.e.*, a single volume element of uniform temperature and density), and is designed to conveniently calculate plasma properties over a grid of input parameters (*e.g.*, T, ρ). PrismSPECT is typically used by experimentalists to infer plasma conditions from spectroscopic measurements.

* In LTE plasmas, atomic level populations depend only on the local temperature (T) and density (ρ). LTE equation-of-state properties and opacities can then be obtained from table look-up (given T, ρ). The atomic level populations of non-LTE plasmas – subject to non-local radiation fields and/or time-dependent ionization effects – must be determined from collisional-radiative modeling.

For a given plasma distribution, SPECT3D computes images and spectra by solving the radiative transfer equation along an array of lines-of-sight extending through the plasma. For both SPECT3D and PrismSPECT, opacities and emissivities in each volume element can be computed for either LTE or non-LTE plasmas. For non-LTE plasmas, atomic level populations are computed by solving a coupled set of atomic rate equations. Both applications support the calculation of time-dependent and steady-state atomic level populations. The atomic rate equations include contributions from: electron-impact ionization, recombination, excitation, and deexcitation for either Maxwellian or non-Maxwellian electron distributions, radiative recombination, spontaneous decay, dielectronic recombination, autoionization, electron capture, photoionization, photoexcitation, and simulated recombination and deexcitation. Line profiles include the effects of Doppler, Stark, natural, Auger, and opacity broadening. Continuum lowering effects are modeled using an occupation probability model,[20] supplemented by the ionization potential depression formalism of More.[21] The occupation probability model produces a continuous reduction in the effective statistical weights of energy levels with increasing density, so that the relatively high-*n* states (*n* = principal quantum number) cannot be populated at high densities.

PrismSPECT, and SPECT3D are currently capable of performing non-LTE atomic kinetics calculations with up to ~ 10^4 – 10^5 discrete atomic energy levels, while HELIOS-CR is limited to ~ 10^3 discrete levels. Atomic models – *i.e.,* a selected set of atomic energy levels and a specification of how the levels are split (*e.g.*, configuration averaged, L-S term split, or fine structure split) – can be chosen from a collection of default models, or users can generate their own customized atomic models. To facilitate the generation of customized atomic models, the AtomicModelBuilder application was developed to conveniently allow users to select energy levels from the atomic data library and to specify the degree of level splitting.

HELIOS-CR, SPECT3D, and PrismSPECT include graphical user interfaces for setting up simulations, online documentation, and interactive graphics packages for viewing space-, time-, and frequency-dependent results. HELIOS-CR conveniently interfaces with SPECT3D and other plasma simulation tools used in analyzing experiments. Each code has been developed to run on Windows, Linux, and Mac OSX platforms.

3. ATOMIC PHYSICS CALCULATIONS

Atomic cross section data generated for Li[6,13] and Sn were computed using the ATBASE suite of codes.[23] Energy levels, photoionization cross sections, oscillator strengths, and autoionization rates are calculated using a configuration interaction model with Hartree-Fock wavefunctions. Collisional coupling between states is complete – *i.e.,* all thermal (non-autoionizing) and autoionizing states are collisionally coupled – with electron-impact collisional excitation and ionization cross sections computed using a distorted wave model. Dielectronic recombination processes involving autoionization states of Ne-like ions and higher are treated explicitly, with electron capture rates determined from detailed balance with their corresponding autoionization rates. For ions with more than 10 bound electrons, autoionization states are not explicitly included in the atomic model, and effective dielectronic recombination rates are utilized.

For high-Z plasmas like Sn, at plasma conditions typical of EUVL radiation sources, there are two major challenges in computing accurate opacities. Firstly, there is a very large number of configurations with open *d* and *f* subshells that can contribute to the opacity. For instance, the number of lines in a single transition array of the type $p^{m+1}d^n \rightarrow p^m d^{n+1}$ or $d^{m+1}f^n \rightarrow d^m f^{n+1}$ can be ~ 10^4 - 10^5. The primary 13.5 nm emission feature from Sn arises from $4p-4d$ and $4d-4f$ transitions. Since all the n = 4 suborbitals in moderately ionized Sn (~ Sn^{10+}) are close in energy, many of the configurations of type $4p^{\omega}4d^n4f^m$ lie well below the ionization threshold, and can potentially have significant contributions to the 13.5 nm emission feature. The shape of the 13.5 nm feature is sensitive to the selected

configurations included in the model. In our calculations, all doubly excited configurations of the type $4p^{\omega}4d^{n}4f^{m}$ are included to ensure accurate treatment of the 13.5 nm emission from Sn. For example, in Sn^{10+} a total of 57 electronic configurations of this type are included in our calculations. We then extended this configuration list to include all higher-*n* outer shell excited-state configurations with principal quantum number up through *n* = 9. The number of electronic configurations considered for Sn^{10+} is ~ 500. The number of transitions in this single ion is ~ 10^6.

Secondly, both relativistic and configuration interaction (CI) effects are important and must be taken into account in determining the line positions and intensities for the transition arrays of interest. An example illustrating the importance of configuration interaction effects is shown in Figure 1, where the calculated line energies and strengths of the mixed transition array $4p^6 4d^4 \rightarrow (4p^6 4d^3 4f^1 + 4p^5 4d^5)$ in Sn^{10+} are shown (*gf* represents the statistical weight of the upper state times the oscillator strength). The upper plot in Fig. 1 is a superposition of the independent arrays $4p^6 4d^4 \rightarrow 4p^6 4d^3 4f^1$ and $4p^6 4d^4 \rightarrow 4p^5 4d^5$, computed in the single configuration approximation. Here, it is seen that both arrays overlap strongly, and that strong transitions are spread out over the wavelength range of 13.0 – 16.5 nm. The lower plot presents the transition lines of the mixed array – that is, $4p^6 4d^4 \rightarrow (4p^6 4d^3 4f^1 + 4p^5 4d^5)$ – computed with configuration interaction effects taken into account. The difference between the two results is significant, as it shows that the strongest lines emit in a relatively narrow wavelength range. Configuration interaction effects result in the reduction in the strengths of some lines, and in increased contributions from different configurations. The array $4p^6 4d^4 \rightarrow 4p^6 4d^3 4f^1$ is partially quenched by the $4p^6 4d^4 \rightarrow 4p^5 4d^5$ array. The net result is a much narrower transition band centered at 13.5 nm. We note that our relativistic CI results for the quenching of transition arrays through configuration mixing are consistent those reported by Bauch *et al.*[24] for Pr ions with close-lying energy levels with 4ℓ orbitals.

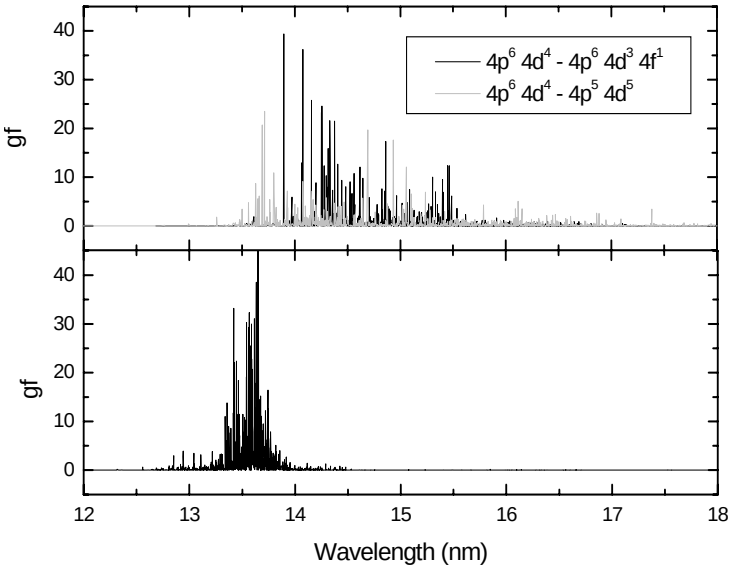

Figure 1. Wavelength-dependent line strengths (gf values) for transition array of Sn^{10+}. Top: superposition of independent transition arrays $4p^6 4d^4 \rightarrow 4p^6 4d^3 4f^1$ and $4p^6 4d^4 \rightarrow 4p^5 4d^5$. Bottom: mixed transition array $4p^6 4d^4 \rightarrow (4p^6 4d^3 4f^1 + 4p^5 4d^5)$ computed with configuration interaction effects included.

In generating our Sn atomic database, fully relativistic CI calculations have been carried out to compute in detail lines contained in more than fifty thousand transition arrays distributed over the 20 lowest ionization stages of tin. In the entire Sn model, a total of ~ 400,000 fine-structure atomic energy levels distributed over all ionization states of tin were computed. For each level, detailed configuration interaction calculations were performed both for low-lying and excited energy levels, which is required in order to accurately compute transition energies, and therefore to accurately predict the shape of the radiation emission band near 13.5 nm. In these calculations, significantly more detail – in terms of energy levels and configuration interactions – was utilized in the modeling of ionization stages below Sn^{19+}. A total of ~ 5 x 10^6 oscillator strengths and transition energies were computed in this model.

Figure 2 shows calculated wavelength-dependent opacities for tin at a mass density of 10^{-3} g/cm^3 and for temperatures ranging from T = 20 to 40 eV. Note that the opacities in the plot on the left are on a logarithmic scale. The $4p-4d$ and $4d-4f$ transitions are the dominant transition arrays in the spectrum.

Prior to performing radiation-hydrodynamics simulations, opacity data tables are generated with 10,000 frequency groups over a grid of temperature and density points. In utilizing these data tables, HELIOS re-groups the opacities according to the user-specified frequency grid. This allows spectral regions of interest to be accurately modelled using a moderate number of frequency groups.

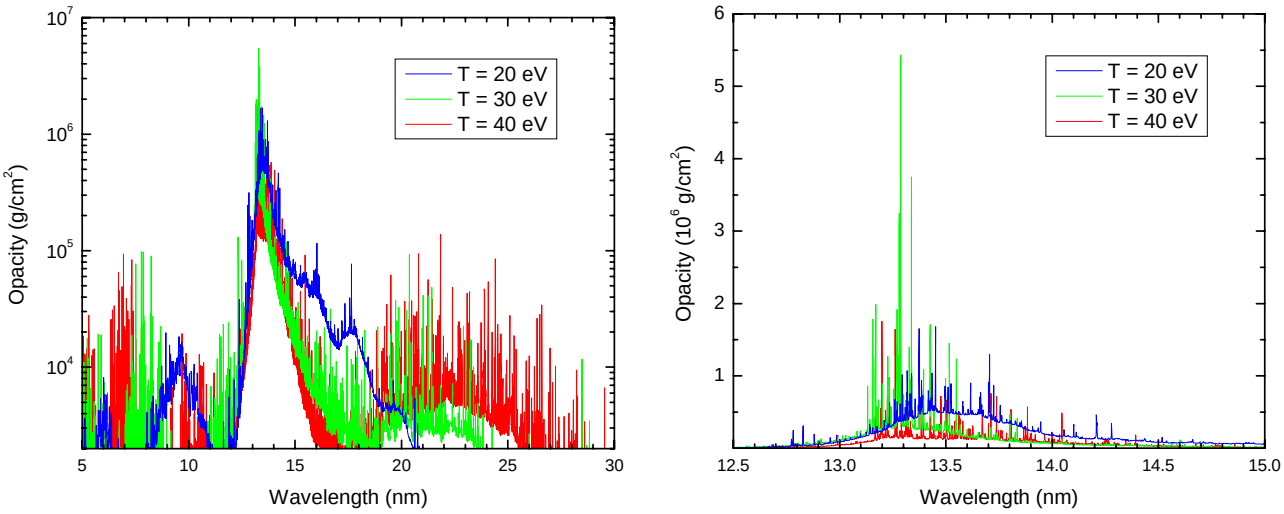

Figure 2. Calculated opacity vs. wavelength for tin plasmas at $\rho = 10^{-3}$ g/cm^3 and temperatures ranging from 20 to 40 eV. The plot on the right shows the opacity on a linear scale in a relatively narrow spectral region near 13.5 nm.

4. SIMULATION OF TIN LASER-PRODUCED PLASMAS

In this section, we describe simulations of tin LPPs. In particular, we: (i) compare simulated frequency-dependent radiation fluxes from HELIOS-CR with spectra obtained from GEKKO XII experiments involving spherical tin-coated targets; (ii) compare calculated 13.5 nm conversions efficiencies (CEs) with experimental values for planar Sn targets; (iii) examine the sensitivity of the 13.5 nm CEs to laser wavelength, intensity, and pulse width; (iv) examine plasma conditions attained in the hot radiating region of the plasmas; and (v) discuss the effect of the thickness of the hot radiating tin plasma on the CE and overall radiation losses from the plasma.

4.1. Comparison with spherical Sn target spectra

As a test of the reliability of HELIOS and the Sn atomic data, we compared results from a series of HELIOS simulations with spectra obtained in spherical target experiments performed at the GEKKO XII laser facility at Osaka.[7,8] In these experiments, 700 μm-diameter CH spheres coated with 1 μm-thick layers of tin were spherically illuminated with the 12 GEKKO laser beams. Gaussian laser pulses with a FWHM of 1.2 ns and wavelength of λ_L = 1.06 μm were used, with the laser intensity being varied from 0.09 to 0.9 TW/cm^2. A comparison of the simulated emergent spectra is shown in Figure 3, where the time-integrated fluxes from the HELIOS simulations (right plots) are shown with the time-integrated spectral measurements (left plots) at each laser power. The overall agreement is seen to be good. In particular, the shape of the main emission feature between 12 nm and 18 nm – which arises primarily due to $4p-4d$ and

$4d-4f$ transitions – agrees very well with the experimental data for all 3 laser intensities (see Section 4.3 for a discussion on how the thickness of the hot plasma affects the shape of the emission feature near 13.5 nm). In these simulations, the calculated 13.5 nm CE ranged from 2.2% to 3.4%, which is consistent with the experimental estimates.[7] The emission at shorter wavelengths is primarily due to relatively high ionization stages of tin ($\gtrsim Sn^{20+}$). The lower calculated intensities could potentially be due to our atomic model currently have less detail for these high ionization stages. However, the experimental intensity scale is not well-defined, and it is unclear whether the spectral intensity of the 1 - 3 nm feature, as defined in power per eV, is actually comparable to the intensity of the 13.5 nm feature.

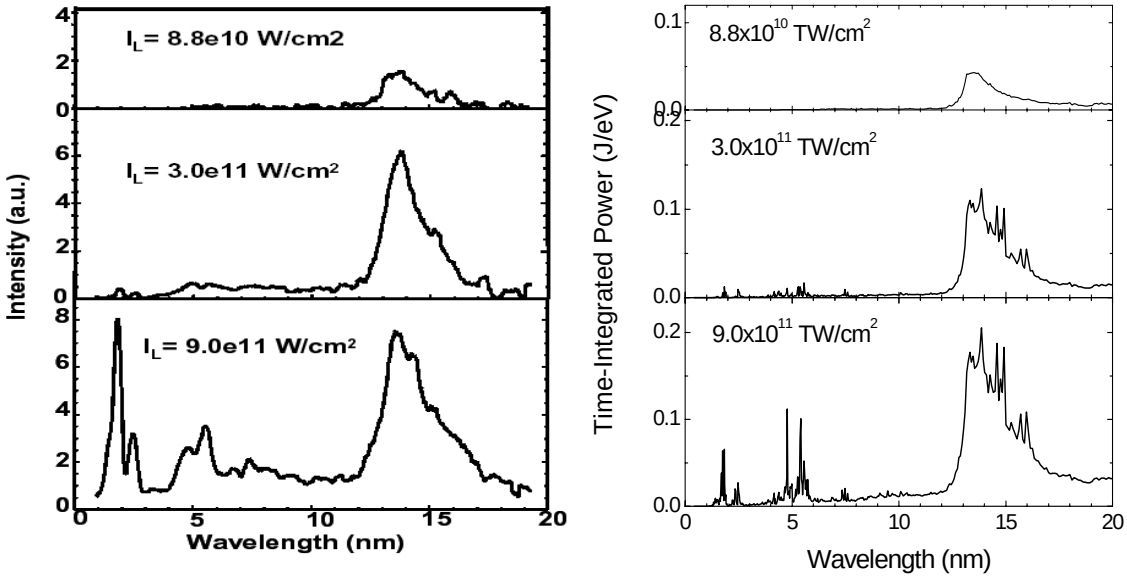

Figure 3. (Left) Time-integrated tin spectra obtained from GEKKO XII experiments[7] of tin-coated spheres at 3 laser powers. (Right) Calculated time-integrated radiative power from HELIOS-CR calculations. The calculated spectra do not include instrumental broadening.

Figure 4 shows the 13.5 nm monochromatic image calculated by post-processing the radiation-hydrodynamics simulations with SPECT3D. The image clearly shows significant limb brightening (*i.e.*, the intensity is brightest at the edges of the spherical plasma).

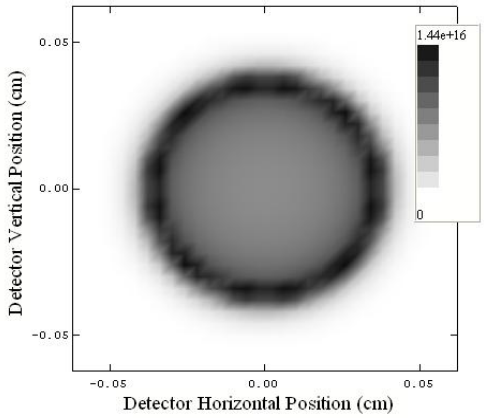

Figure 4. Calculated 13.5 nm monochromatic image at a time near peak laser power. The darker portions of the image correspond to higher intensities. (Small deviations from symmetry appear due to the rectangular grid of lines-of-sight used for the virtual detector.)

The above simulations of the GEKKO XII experiments show overall good agreement with the measured spectra. The calculated shape of the 13.5 nm feature is very similar to the experimental shape. This is important because for plasma conditions relevant to Sn EUV lithography LPPs, the radiation losses from the main emission feature at 12 - 18 nm represent a large fraction of the overall radiation losses. And it is only radiation within a ~ ± 1% band that contributes to the conversion efficiency. Outside of this band (*e.g.,* at λ = 15 nm), the radiated energy does not contribute to useful energy for the EUVL system.

4.2. Comparison of calculated and experimental conversion efficiencies for planar Sn targets

Tin LPP experiments were performed at Cymer, Inc.,[15] in which Sn planar foils were irradiated by 0.35 μm and 1.06 μm laser light with pulse lengths of 10 ns and 1 ns, respectively. Results from these experiments are shown in Figure 5. The results correspond to measurements taken in a 2% bandwidth at 13.5 nm, and for a detector located at an angle of 22 degrees with respect to the laser-target axis. The measured conversion efficiencies are obtained assuming the radiation from the plasma is emitted uniformly into 2π steradians.

Fig. 5 shows the peak value for the experimentally-measured CE is 4.5% in the 1.06 μm laser case, and occurs at a incident laser intensity of 1.5 x 10^{11} W/cm^2. In the 0.35 μm laser case, CEs were measured for planar targets located either after the laser focus (filled squares) or before the laser focus (open squares). In the latter case, the experimental CEs tend to be somewhat higher at laser intensities $\lesssim 10^{11}$ W/cm^2. One possible explanation for this is that in the case where the target is located before the laser focus, the target plasma effectively sees the laser spot size increase as it expands outward (toward the beam). In this case, hot plasma expanding radially away from the beam-target axis continues to be heated by the beam, whereas the opposite is true when the target is located after the laser focus.

Results from HELIOS simulations for this series of experiments are also shown in Figure 5. For the 1.06 μm laser case, the HELIOS results predict that a peak CE of just below 4% occurs at a laser intensity of 0.8 x 10^{11} W/cm^2. The overall intensity dependence of the CE is in good agreement with experimental measurements, particularly at intensities $\lesssim 10^{11}$ W/cm^2. At higher laser intensities, both the experimental and calculated CEs are seen to decrease as the laser intensity increases, but with the calculated CEs decreasing more rapidly. One possible explanation for this is that the temperatures in the higher intensity simulations are sufficiently high that the mean ionization state of the tin exceeds Sn^{20+}. At these higher ionization stages, the level of detail included in our current atomic model is less than that for ionization stages below Sn^{20+}. Alternatively, it is possible that non-LTE effects may be playing a role. At relatively high temperatures and low densities in plasmas, radiative and dielectronic recombination rates can exceed collisional (3-body) recombination rates, resulting in a lower mean ionization state than that of a plasma in LTE. In this case, it is possible that the calculated mean ionization in the high laser intensity cases is being overestimated, resulting in lower CEs than the experimental values.

For the 0.35 μm laser case, the HELIOS results predict a peak CE of ~ 1%, which remains relatively flat for laser intensities from ~ 4 x 10^{10} W/cm^2 to 8 x 10^{11} W/cm^2. Here the agreement between simulation and experiment is seen to be very good over a wide range of intensities. For these shorter wavelength calculations, the agreement at higher intensities may be better than in the 1.06 μm case because for a given intensity, the temperatures and mean ionization state in the shorter wavelength cases are lower due to the deeper penetration of the laser light (*i.e.,* more mass is being heated). In short, we find the overall agreement between the HELIOS simulations and experimental CE measurements to be very good.

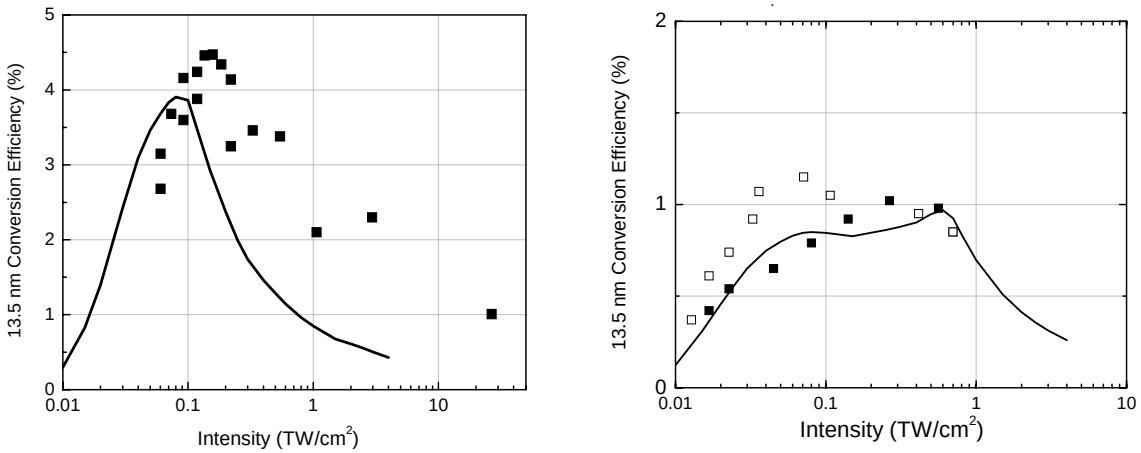

Figure 5. Comparison of calculated and experimentally measured 13.5 nm conversion efficiencies for planar tin targets. Left: calculated (solid curve) and experimental (filled squares) results for 1.06 μm, 1 ns laser pulses. Right: calculated (solid curve) and experimental (open and filled squares) results for 0.35 μm, 10 ns laser pulses. The open square correspond to experiments in which the target was positioned in front of the laser focus.

4.3. Dependence of Sn LPP conversion efficiency on laser parameters

In this section, we present results from a series of HELIOS simulations for Sn laser-produced plasmas irradiated by 1.06 μm laser light. In this series of calculations, the laser intensity profile was flat-topped, with a 0.1 ns rise time at the beginning and a 0.1 ns fall off at the end of the pulse. The peak laser intensity was varied from 1 x 10^9 to 6.4 x 10^{11} W/cm^2. The pulse width was varied between 0.1 and 10 ns. For each set of laser parameters, a HELIOS simulation was performed for a Sn planar foil. Radiation transport was computed using a multi-angle model with a total of 200 frequency groups, with finer resolution around 13.5 nm. Multigroup opacities were based on atomic data described in Section 3, and assumed LTE atomic level populations.

In each calculation, we recorded the conversion efficiency in a Gaussian-shaped band centered at 13.50 nm. The FWHM was 2% of the band central wavelength. Figure 6 shows the computed 13.5 nm CEs as a function of laser intensity. For the λ_L = 1.06 μm laser series, the conversion efficiencies peak at ~ 4%. The peak value of the CE for each curve, as well as the laser intensity at which the peak occurs, shows a modest dependence on the pulse width in this series.

It is informative to examine how the overall energetics of the plasma varies with laser parameters. Figure 7 shows, for the λ_L = 1.06 μm series, the fraction of laser energy that is converted to radiation reemitted by the plasma (left) and the amount of energy converted into fluid kinetic energy (right). As the laser intensity is increased, a higher proportion is converted into radiation. This is expected because higher temperature plasmas tend to be stronger radiators. As more and more energy is converted into radiation losses, less and less energy is available to be converted into kinetic energy. Fig. 7 also shows that as the laser pulse length increases, more energy is converted into radiation. This may be due to the fact that at late times the laser energy is deposited in the expanding hot plasma, as opposed to heating an initially cold material which would require energy to heat and ionize it.

The time-dependence of the energy partitioning between plasma internal energy, fluid (*i.e.*, debris ion) kinetic energy, and radiation losses is shown in the left plot of Figure 8 for the case with a 1.06 μm, 0.08 TW/cm^2, 3 ns laser pulse. It is seen that by 10 ns, 58% of the incident laser energy has been radiated away from the plasma. By comparison, 26% is in

fluid kinetic energy at this time, and 16% is in plasma internal energy (thermal plus ionization/excitation). At late times, much of the remaining internal energy will be converted to debris kinetic energy as the plasma continues to cool and expand.

To examine the characteristics of the radiation as it propagates through the plasma, we used SPECT3D to post-process the HELIOS results for this case. Results for the depth dependence of the temperature, electron density, specific intensities, and optical depths are shown in the right plots in Figure 8. Here, we represent the depth by the areal mass ($= \int \rho \, dr$) to provide greater insight as to the amount of mass contributing to the radiative emission. Note that in this 1.06 μm laser case, the thickness of the emitting layer, as measured in terms of the areal mass. is ~ 2 x 10^{-5} g/cm^2. This is the width of the region of relatively hot temperatures (T ~ 30 - 40 eV, upper right plot in Fig. 8) and the region where the photons in the 13.5 nm spectral region are born, as can be seen in the intensity plot (center right plot). This thickness is influenced by the depth at which the laser energy is deposited.

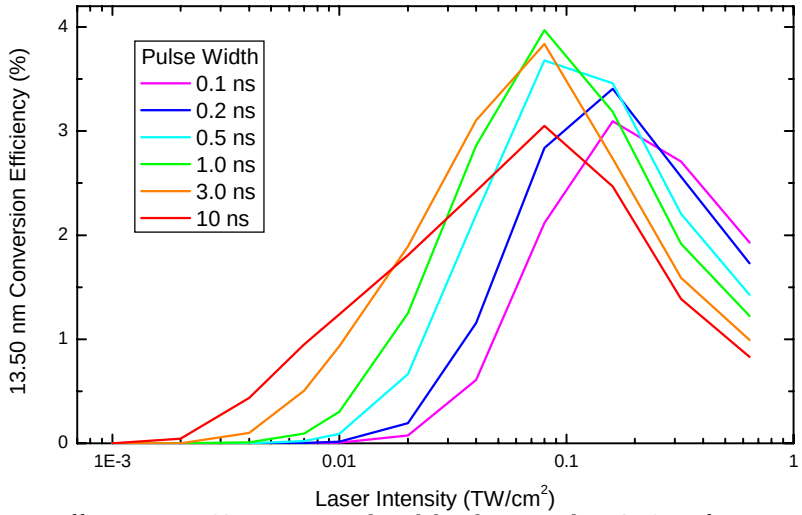

Figure 6. Calculated conversion efficiencies in 2% FWHM wavelength bands centered at 13.50 nm from HELIOS simulations of Sn laser-produced plasmas with λ_L = 1.06 μm laser.

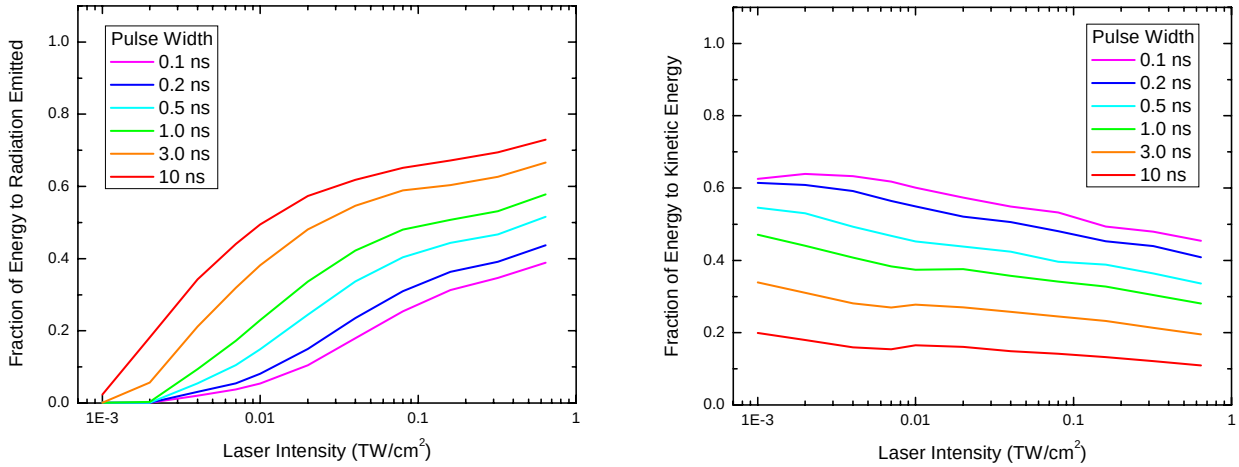

Figure 7. Calculated fraction of laser energy escaping plasma in the form of radiation (left), and converted into fluid kinetic energy (right) from HELIOS simulations with a λ_L = 1.06 μm laser. Energies correspond to those tabulated at a simulation time of 15 ns. The remaining energy at this time is in the form of plasma internal energy.

Figure 9 (left plot) shows the time-integrated spectral emission calculated in the two HELIOS simulations for the 1.06 μm, 0.08 TW/cm^2, 3 ns laser case, as well as the result from a 0.35 μm, 0.32 TW/cm^2, 10 ns case. Note that the emission feature near 13.5 nm is not as sharply peaked in the λ_L = 0.35 μm case (red curve). Of the energy lost from the plasma in the form of radiation, a greater fraction is emitted in a narrow band near 13.5 nm in the λ_L = 1.06 μm case. Energy radiated at longer wavelengths (λ ~ 14 to 16 nm) is in a sense wasted energy as it results in the plasma losing energy (*i.e.*, it decreases the temperature) and does not contribute to useful energy for EUVL systems.

The effect of thickness on the spectral emission from the tin plasma can be seen more clearly in the right plot in Figure 9, where we show spectra for simple uniform temperature and density plasma slabs of Sn computed using PrismSPECT. In each case, the plasma temperature is T = 25 eV, and mass density is ρ = 1 x 10^{-4} g/cm^3. For the case in which the plasma thickness is $\rho \Delta L$ = 0.5 x 10^{-5} g/cm^3 (*i.e.*, ΔL = 0.05 cm), the emission feature near 13.5 nm is strongly peaked (red curve). As this plasma thickness increases to $\rho \Delta L$ = 2 x 10^{-5} g/cm^3 – which is similar to the thickness obtained in the λ_L = 1.06 μm, P_L = 0.08 TW/cm^2, 3 ns laser beam case – there is considerably more emission at λ ~ 14 to 16 nm. At λ ~ 13.2 - 13.5 nm, the optical depth (*i.e.*, the opacity due to 4*f* - 4*d* and 4*d* - 4*p* transitions in Sn) is sufficiently large that the intensity approaches the Planckian intensity. These PrismSPECT simulations suggest that thin plasma radiation layers should be most effective for EUVL systems, as they produce less "wasted" radiation.

5. SUMMARY

We have performed calculations for tin laser-produced plasmas at conditions relevant to EUV lithography radiation sources using a suite of plasma simulation tools. Detailed atomic physics calculations for Sn were performed including relativistic and configuration interaction effects to determine the transition energies and oscillator strengths for ~ 10^6 -10^7 lines in transition arrays of moderately-ionized Sn, with special emphasis on those contributing to the main 13.5 nm emission feature in Sn LPP experiments. Using the results of these atomic physics calculations, we performed a series of radiation-hydrodynamics simulations for Sn LPPs to examine the dependence of the 13.5 nm conversion efficiency on the laser intensity, wavelength, and pulse length. Comparisons of simulation results with previously published spectra were presented, along with comparisons of calculated 13.5 nm conversion efficiencies with data obtained in experiments performed at Cymer, Inc.

Our calculations typically find Sn LPP conversion efficiencies of ~ a few percent, ranging up to ~ 1 - 2% for 0.35 μm laser pulses and up to ~ 4% for 1.06 μm laser pulses. We note that the calculations reported here are based on simple flat-topped laser pulses, and that it may be possible to further enhance 13.5 nm CEs by using shaped laser pulses and/or different laser wavelengths.

Comparison between calculated 13.5 nm conversion efficiencies and experimentally measured values in 0.35 μm and 1.06 μm laser experiments showed good general agreement. At laser intensities above 10^{11} W/cm^2 in the 1.06 μm case, the calculations predict somewhat lower CEs than experiments. It is believed that this may be due to either insufficient detail in our atomic models for ionization stages above Sn^{20+}, or the possibility of non-LTE effects leading to plasma ionization states lower than those predicted in our simulations. The simulation codes described in this paper support the modeling of non-LTE plasmas, and it is expected that these issues will be addressed in future work.

Finally, another important issue for EUVL systems concerns the characteristics of the debris ions (or ablated target mass), and their potential for damaging the EUVL optics system. HELIOS radiation-hydrodynamics simulations predict the total amount of energy converted into kinetic energy, as well as the energy (*i.e.*, velocity) distribution of the ablated target mass. These predictions for the debris ion energy spectrum will be utilized in future debris ion studies.

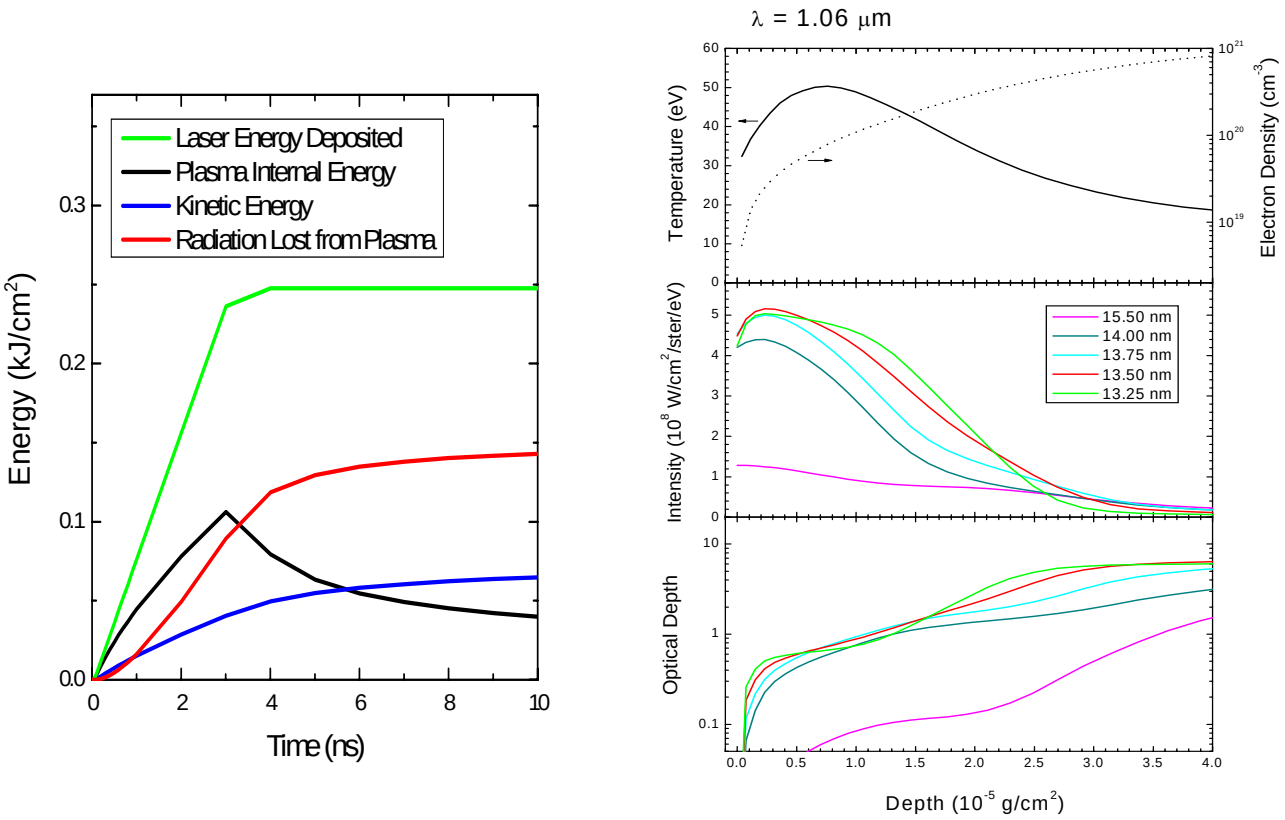

Figure 8. Results from the simulation of a Sn target heated by a 1.06 μm, 0.08 TW/cm^2, 3 ns laser beam. Left: Energy partitioning as a function of time. Right: Temperature, electron density, specific intensity, and optical depth computed with HELIOS and SPECT3D for a line-of-sight at normal incidence to the Sn planar foil. Results correspond to a simulation time of 3 ns. Specific intensities at selected wavelengths are in the direction of the plasma boundary to the left. Optical depths are measured from the left boundary at selected wavelengths.

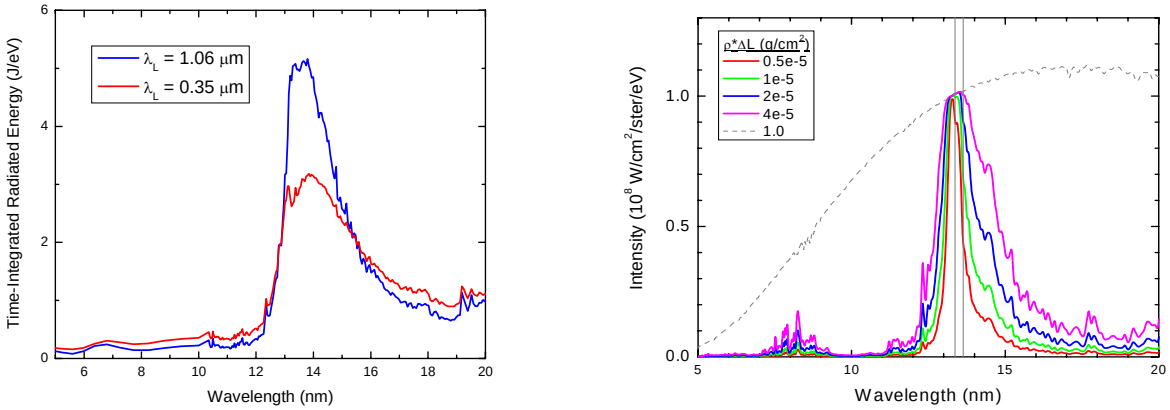

Figure 9. Left: Comparison of calculated time-integrated spectra from HELIOS simulations of Sn LPPs with a λ_L = 0.35 μm, P_L = 0.32 TW/cm^2, 1 ns laser beam (red curve), and with a λ_L = 1.06 μm, P_L = 0.08 TW/cm^2, 3 ns laser beam (blue curve). Right: Spectra computed using PrismSPECT for a uniform density (ρ = 10^{-4} g/cm^3), isothermal (T = 25 eV) Sn planar plasma of varying thickness. Note that the width of the emission feature near 13.5 nm increases as the thickness of the emitting plasma increases. At very large thicknesses ($\rho\,\Delta L$ = 1 g/cm^2), the emission spectrum approaches a Planckian spectrum. A bandwidth of 2% is shown for reference.

ACKNOWLEDGEMENTS

This work was supported in part by Cymer, Inc.

REFERENCES

1. Y. Watanabe, K. Ota, and H. Franken., "Source Requirements for EUV Lithography," SEMATECH International EUV Source Workshop, Santa Clara, CA (2004).
2. U. Stamm, *et al*., "High Power EUV Sources for Lithography – A Comparison of Laser-Produced Plasma and Gas Discharge Produced Plasma," Proc. SPIE **4688**, 133, Emerging Lithographic Technologies VI (2002).
3. C. Rettig, I. Fomenkov, and J. J. MacFarlane, "Computational Predictions of Laser-Produced Plasma EUV Source Performance," EUV Source Modeling Workshop, Miyazaki, Japan (2004).
4. M. Richardson, C. S. Koay, K. Takenoshita, C. Keyser, and M. Al-Rabban, "High Conversion Efficiency Mass-Limited Sn-Based Laser Plasma Source for Extreme Ultraviolet Lithography," J. Vac. Sci. Technol. B **22**, 785 (2004).
5. G. O'Sullivan, "EUV Emission from Xe and Sn Plasmas," Second International Symposium on EUV Lithography, Antwerp, Belgium (2003).
6. J. J. MacFarlane, I. E. Golovkin, P. R. Woodruff, "Preliminary Analysis of Laser-Produced Lithium Plasmas," Prism Computational Sciences Report PCS-R-052 (2004).
7. K. Fujima, *et al*., "Theoretical Simulation of Extreme UV Radiation Source for Lithography," Proc. SPIE **5374**, 405, Emerging Lithographic Technologies VIII (2004).
8. H. Nishimura, *et al*., "Characterization of Extreme UV Radiation in Laser-Produced Plasma for Use in Lithography," Proc. Inertial Fusion and Sciences Applications 2003, 1077, Amer. Nucl. Soc. (2004).
9. C. S. Koay, K. Takenoshita, C. Keyser, and M. Al-Rabban, "High Conversion Efficiency Mass-Limited Sn-Based Laser Plasma Source for Extreme Ultraviolet Lithography," J. Vac. Sci. Technol. B **22**, 785 (2004).
10. U. Stamm, *et al.*, "EUV Source Power and Lifetime: The Most Critical Issues for EUV Lithography," Proc. SPIE **5374**, 133, Emerging Lithographic Technologies VIII (2004).
11. H. Komori, *et al.*, "Laser-Produced Plasma Light Source Development for Extreme Ultraviolet Lithography," J. Vac. Sci. Technol. B **21**, 2843 (2003).
12. J. J. MacFarlane, P. Wang, P. R. Woodruff, and I. E. Golovkin, "Preliminary Simulations of Laser-Produced Tin Plasmas," Prism Computational Sciences Report PCS-R-055 (2004).
13. J. J. MacFarlane, I. E. Golovkin, and P. R. Woodruff, "Simulation of Laser-Produced Lithium Plasmas in Support of Cymer EUVL Experiments," Prism Computational Sciences Report PCS-R-053 (2004).
14. A. Hassanein, V. Sizyuk, V. Tolkach, V. Morozov, T. Sizyuk, B. Rice, and V. Bakshi., "Simulation and Optimization of DPP Hydrodynamics and Radiation Transport for EUV Lithography Devices," Proc. SPIE **5374**, 413, Emerging Lithographic Technologies VIII (2004).
15. J. Hoffman, *et al.*, "LPP EUV Conversion Efficiency Optimization," this proceedings (2005).
16. I. Fomenkov, R. Oliver, S. Melnychuk, N. Bowering, R. Ness, O. Khodykin, C. Rettig, "Dense Plasma Focus Device as a Light Source for EUV Lithography," EUV Source Workshop, Santa Clara, CA (2002).
17. Additional information on major features of these plasma simulation tools is provided at http://www.prism-cs.com.
18. J. J. MacFarlane, I. E. Golovkin, and P. R. Woodruff, "HELIOS-CR – A 1-D Radiation-Magnetohydrodynamics Code with Inline Atomic Kinetics Modeling," J. Quant. Spectrosc. Radiat. Transfer, in press (2005).
19. S. P. Lyon, J. D. Johnson, "SESAME: The Los Alamos National Laboratory Equation of State Database," Technical report LA-UR-92-3407, Los Alamos National Laboratory, Los Alamos, NM (1992).
20. D. G. Hummer, and D. Mihalas, "The Equation of State for Stellar Envelopes. I. An Occupation Probability Formalism for the Truncation of Internal Partition Functions," Astrophys J. **331**, 794 (1988).
21. R. M. More, *Applied Atomic Collision Physics, vol. 2*, Academic Press, New York (1982).
22. J. J. MacFarlane, I. E. Golovkin, P. R. Woodruff, D. R. Welch, B. V. Oliver, T. A. Mehlhorn, R. B. Campbell, "Simulation of the Ionization Dynamics of Aluminum Irradiated by Intense Short-Pulse Lasers," Proc. Inertial Fusion and Sciences Applications 2003, **457**, Amer. Nucl. Soc. (2004).
23. P. Wang, "Computation and Application of Atomic Data for Inertial Confinement Fusion Plasmas," Ph.D. dissertation, Dept. of Nuclear Engineering and Engineering Physics, Univ. of Wisconsin, Madison, WI (1991).
24. J. Bauche, C. Bauche-Arnoult, M. Klapisch, P. Mandelbaum, and J. L. Schwol, "Quenching of Transition Arrays through Configuration Mixing," J. Phys. B **20**, 1443 (1987).